

Research Paper

Stable CuSiBeta prepared by direct ion-exchange approach for methanol steam reforming to produce hydrogen

Yang Hong^{a,b}, Chao Ma^{a,b,c}, Nana Yan^a, Peng Guo^{a,b,*}, Zhongmin Liu^{a,b}^a National Engineering Research Center of Lower-Carbon Catalysis Technology, Dalian Institute of Chemical Physics, Chinese Academy of Sciences, Dalian, Liaoning 116023, China^b University of Chinese Academy of Sciences, Beijing 100049, China^c School of Chemistry, Dalian University of Technology, Dalian, Liaoning 116024, China

ARTICLE INFO

Keywords:

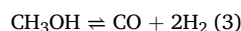
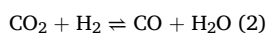
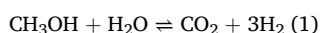
Pure-silica *BEA zeolite
Ion-exchange
Methanol steam reforming
Silanol nests

ABSTRACT

The methanol steam reforming (MSR) is a potential route to produce hydrogen from methanol and water, in which the Cu-based catalysts exhibit high activity and hydrogen selectivity. However, the Cu-based catalysts suffer from severe deactivation because of the rapid sintering of the copper species in the reaction. In this study, high loading and highly dispersed copper species stabilized by *BEA-type pure-silica zeolites were prepared with a direct ion exchange approach and applied as stable catalysts for MSR. The *BEA-type pure-silica zeolites were synthesized by a green synthetic methodology called OSDA-mismatch approach without utilizing the toxic HF or post-acid aluminosilicate seeds. Among Cu-based zeolite catalysts, the 6.0CuSiBeta (6 wt% Cu content) exhibits better activity and stability, achieving 80% methanol conversion over 100 h with a WHSV of 8.0 mL/g/h. Comprehensive and thorough characterizations reveal that the silanol nests in *BEA-type pure-silica zeolites can not only improve the dispersion of copper species and inhibit the sintering of copper in the reaction.

1. Introduction

Hydrogen produced from renewable resource is considered as an important and environmentally friendly energy carrier. However, the storage and transportation of the gaseous hydrogen is still an enormous challenge because of the physical properties, such as small molecular and low explosive limit [1,2]. Therefore, the liquid organic hydrogen carriers (LOHC) such as alcohol, N-heterocycles, and cycloalkanes, are proposed to storage and transport hydrogen [3,4]. Among these organics, the methanol is the most potential candidate due to its high H/C ratio, high-volume energy density, no strong C-C bonds, and easily storage and transportation [5–7]. Given these approaches to produce hydrogen from the methanol, the methanol steam reforming (MSR) is the most promising one with a low reaction temperature and a high hydrogen selectivity [8–12]. Besides MSR, there are two side reactions occur simultaneously, one is the water gas shift (WGS) and the other is the methanol decomposition (MD), as shown in Eqs. (1)–(3):



The MSR catalysts can be generally categorized into two types, noble metal (Pd, Pt, and Ru) and Cu-based catalysts [13–20]. Among these catalysts, Cu-based catalysts have drawn lots of attentions on account of the low cost, the high activity, and the excellent selectivity. Nevertheless, due to the low Tammann temperature, the Cu-based catalysts commonly suffer from severe thermal sintering leading to the poor stability. To enhance the sintering resistance of Cu-based catalysts, researchers have introduced amphoteric or basic metal oxides like Al₂O₃, SiO₂, and mesoporous carbon, as well as promoters like ZnO, MgO, and CeO₂ [18,19,21–25]. These additives are used to reduce the size of copper particles and improve their dispersion. Furthermore, the effect of chemical state of copper species has also been explored. Li et al. found that co-feeding hydrogen and methanol steam enhances the interface of Cu/ZnO, thus improving the activity and durability of Cu/ZnO/Al₂O₃ catalysts [26]. Filippo Bossola et al. revealed that the addition of silica (10 wt%) to Cu/ZrO₂ catalysts can control the crystallization of the zirconia and increase the reduction temperature of copper species, which result in highly dispersed and stable copper nanoparticles [27].

* Corresponding author at: National Engineering Research Center of Lower-Carbon Catalysis Technology, Dalian Institute of Chemical Physics, Chinese Academy of Sciences, Dalian, Liaoning 116023, China.

E-mail address: pguo@dicp.ac.cn (P. Guo).

<https://doi.org/10.1016/j.mcat.2024.114436>

Received 14 May 2024; Received in revised form 15 July 2024; Accepted 30 July 2024

Available online 7 August 2024

2468-8231/© 2024 Elsevier B.V. All rights are reserved, including those for text and data mining, AI training, and similar technologies.

An alternative approach for stabilizing copper species is the utilization of pure-silica zeolite matrices. These matrices consist of basic building blocks of SiO₄ tetrahedra, interconnected through shared corner oxygen atoms, forming intricate three-dimensional (3D) channel- or cage-based structures. For instance, in our recent research, we employed a one-pot method to encapsulate copper nanoparticles within the Silicate-1 (MFI-type 10 × 10 × 10-ring pure-silica zeolite) matrix, showcasing its high stability during the MSR reaction [28]. However, using the one-pot method to confine copper nanoparticles in the Silicate-1 matrix results in a limited copper content (approximately a maximum of 2 wt%), consequently restricting the specific reaction rate. Compared with the well-investigated Silicate-1 matrix, the dealuminated zeolite Beta (*BEA-type 12 × 12 × 12-ring pure-silica zeolite) also serves as an effective matrix for encapsulating metal and metal oxide nanoparticles [29–31]. This is due to two main factors: 1) its large pore openings facilitate the diffusion of metal precursors into the interior of the zeolite, and 2) the presence of silanol groups within the zeolite structure aids in stabilizing these nanoparticles. For instance, Li et al. reported that a series of metals and/or metal oxides confined within dealuminated Beta zeolite exhibit notable activity in ethanol conversion [29,32,33]. Unfortunately, such essential pure-silica matrix must undergo post-synthesis acid treatment, which inevitably leads to environmental concerns. Very recently, we reported a novel synthetic methodology called OSDA-mismatch approach for the green synthesis of pure-silica zeolites without aiding toxic fluorides or corresponding seeds [34]. Using this unique approach, fifteen pure-silica zeolites have been successfully prepared within the shorten crystallization time. It is crucial to emphasize that *BEA-type pure-silica zeolite can be synthesized in 66 h without the use of HF or seeds. Moreover, the classical organic structure-directing agent TEA⁺ embedded in the as-made sample, whose positive charges are balanced by silanol groups, can be directly exchanged by inorganic cations. Therefore, the direct incorporation of Zn²⁺ ions into the as-made *BEA-type pure-silica zeolite, synthesized through the OSDA-mismatch approach, resulted in effective performance in propane dehydrogenation.

Herein, we report a highly active and robust Cu-based catalyst with high copper contents confined within the *BEA-type pure-silica zeolite (named 6.0CuSiBeta) for the MSR reaction, exhibiting a durability of 100 h with methanol conversion above 80% at a WHSV of 8.0 mL/g/h. Such catalyst is conveniently synthesized through direct Cu²⁺ ion exchange with the as-synthesized *BEA-type pure-silica prepared by the green synthetic approach, avoiding the environmental concerns such as the utilization of toxic HF or acid post-synthesis. Comprehensive and systematic investigations, characterized by various techniques, reveal that the copper species captured by the silanol nest result in high dispersion in the pure-silica zeolite matrix, with no obvious particles or clusters. This stabilization prevents the easy-sintering of copper species, ultimately enhancing its activity and stability.

2. Experimental section

2.1. Material syntheses

2.1.1. Preparation of CuSiBeta

As-synthesized *BEA-type pure-silica zeolite (designated as SiBeta) was prepared by OSDA-mismatch according to our previous work [34]. Cu²⁺ ions in the aqueous solution are exchanged with the as-synthesized SiBeta samples (containing OSDAs embedded in the microporosity). 1g as-synthesized SiBeta sample was dissolved in 50 mL deionized water and then the Cu(Ac)₂·H₂O was added to the slurry, subsequently the slurry was treated at 80 °C for 4 h. And then the obtained solid washed with deionized water and dried at 100 °C overnight (denoted as xCuSiBeta-IE, where x stands for the Cu loading). After the calcination at 550 °C for 6 h in air flow, the xCuSiBeta catalysts were obtained.

2.1.2. Preparation of Cu/SiBeta-F

The conventional impregnated method was also employed to prepare another MSR catalyst for comparison. The *BEA-type pure-silica zeolite was synthesized in the F medium. The synthesis composition was varied as follows: 1SiO₂: 0.5TEAOH: 0.45NH₄F: 1H₂O [35]. First, the tetraethoxysilane and TEAOH were mixed and stirred for 2 h and then NH₄F was added to the solution. The excess water was evaporated at 80 °C to obtain the final gel, and then the gel was transferred to a Teflon-lined autoclave and reacted at 160 °C for 24 h. After the crystallization completed, the slurry was washed with deionized water three times and dried at 100 °C overnight, following calcined at 550 °C for 6 h. This sample is denoted as SiBeta-F.

Later, 0.18 g Cu(Ac)₂·H₂O were dissolved in 10 mL of water and the 1.0 g obtained SiBeta-F was added into the solution, which was further sonication for 15 min, followed by stirring for 12 h. Thereafter, the suspension was dry at 80 °C, and then calcined at 550 °C for 6 h. The finally obtained sample was named 6.0Cu/SiBeta-F.

2.2. Characterizations

The PANalytical X'Pert PRO X-ray diffractometer with Cu-Kα radiation (λ = 0.15418 nm) was employed to record the XRD patterns, operating at 40kV and 40mA. The elemental analysis of the samples was measured with a PANalytical Axios Advanced X-ray fluorescence (XRF) spectrometer and coupled plasma optical emission spectroscopy (ICP-OES) on an ICP-OES 7300DV instrument (PerkinElmer) with a sensitivity line of 349.8 nm and a detection range of 1–10 ppm.

The surface area and pore volume of the catalysts were calculated using N₂ adsorption-desorption isotherms using a Micromeritics ASAP2020 at -196 °C. The BET equation and t-plot methods were employed to evaluate the total surface area and pore volume, respectively.

The solid-state ²⁹Si MAS NMR spectra were recorded with a spinning rate of 8 kHz using high-power proton decoupling. 800 scans were accumulated with a recycle delay of 60 s. Chemical shifts were referenced to kaolinite at -91.5 ppm.

The UV-vis spectra were collected using VARAIN Cary 5000 UV-vis-NIR with a wavenumber range from 200 to 800 nm, and BaSO₄ was used as background.

The reduction behaviours of the catalysts were analysed with H₂-temperature programmed reduction (TPR) using a chemisorption analyser, Micromeritics AutoChem II 2920, equipped with a thermal conductivity detector (TCD). For H₂-TPR, samples were heated under 10% volume H₂/Ar, and the temperature was programmed to rise from 50 °C to 400 °C at a ramping rate of 10 °C/min. before reduction, the samples were pretreated with Ar at 300 °C for 30 min. The dispersion of Cu species in the catalysts was determined by N₂O chemisorption. The catalysts were heated under 10% H₂/Ar (volume basis), with the temperature ramped from 50 °C to 400 °C at a rate of 10 °C/min. The amount of hydrogen consumed during the initial temperature-programmed reduction (TPR) was denoted as A₁. Subsequently, the reactor was purged with Ar at 50 °C. A flow of 10% N₂O/Ar flow (30 mL/min) was then introduced to oxidize surface Cu atoms to Cu₂O over 30 min at 50 °C. After flushing the reactor with Ar to remove excess oxidant, a second TPR experiment was conducted under 10% H₂/Ar (30 mL/min) until 400 °C. The hydrogen consumption in this second TPR was denoted as A₂. The dispersion of Cu (D_{Cu}) was calculated using the following equation [36]:

$$D_{\text{Cu}} = \frac{2A_2}{A_1} \times 100\%$$

The high-angle annular dark-field scanning transmission electron microscopy (HAADF-STEM), transmission electron microscopy (TEM) images, and Energy dispersive X-ray spectra (EDS-mapping) were taken on JEOL JEM-ARM300F.

The X-ray photoelectron spectroscopy (XPS) analysis was conducted

on an ESCALAB 250Xi spectrometer using an Al K α ($h\nu = 1486.6$ eV) X-ray source with a pass energy of 100 eV, with the base pressure of the analysis chamber less than 1×10^{-8} Pa.

The CO Fourier transform infrared spectroscopy (FTIR) analysis was measured on a BRUKER TENSOR 27 spectrometer. Each spectrum consisted of 32 scans and was collected with a resolution of 4 cm $^{-1}$. The samples were pretreated under N $_2$ at 300 °C for 10 min, and then cooled to room temperature. CO was introduced into the chamber until saturation adsorption occurred, followed by the introduction of N $_2$ to sweep away any unadsorbed CO.

2.3. MSR catalytic test

The MSR reaction was performed in a fixed-bed reactor with an inner diameter of 6 mm. Typically, 0.14 g of the CuSiBeta (40-60 mesh) catalyst was placed in the microtubular reactor. Prior to each reaction, the catalysts were treated with flow nitrogen (34 mL/min) at 320 °C for 30 min, and then the mixture of methanol and water was introduced to the reactor using nitrogen as a carrier gas (34 mL/min). The products were analysed with online gas chromatography (Agilent 7890B) equipped a thermal conductivity detector (TCD) and Porapak QS column. Methanol conversion, product selectivity of products and carbon balance are calculated using the following equation:

$$\text{CH}_3\text{OH Conversion} = \frac{\text{CH}_3\text{OH}_{\text{in}} - \text{CH}_3\text{OH}_{\text{out}}}{\text{CH}_3\text{OH}_{\text{in}}} \times 100\%$$

$$S(\text{H}_2) = \frac{\text{H}_2 \text{ moles in products}}{(\text{H}_2 + \text{CO} + \text{CO}_2) \text{ moles in products}} \times 100\%$$

$$S(\text{CO}_2) = \frac{\text{CO}_2 \text{ moles in products}}{(\text{H}_2 + \text{CO} + \text{CO}_2) \text{ moles in products}} \times 100\%$$

$$S(\text{CO}) = \frac{\text{CO moles in products}}{(\text{H}_2 + \text{CO} + \text{CO}_2) \text{ moles in products}} \times 100\%$$

$$\text{Carbon balance} = \frac{\text{moles of carbon in products}}{\text{moles of carbon in CH}_3\text{OH fed}} \times 100\%$$

3. Result and discussion

3.1. Structural characterizations of fresh CuSiBeta samples

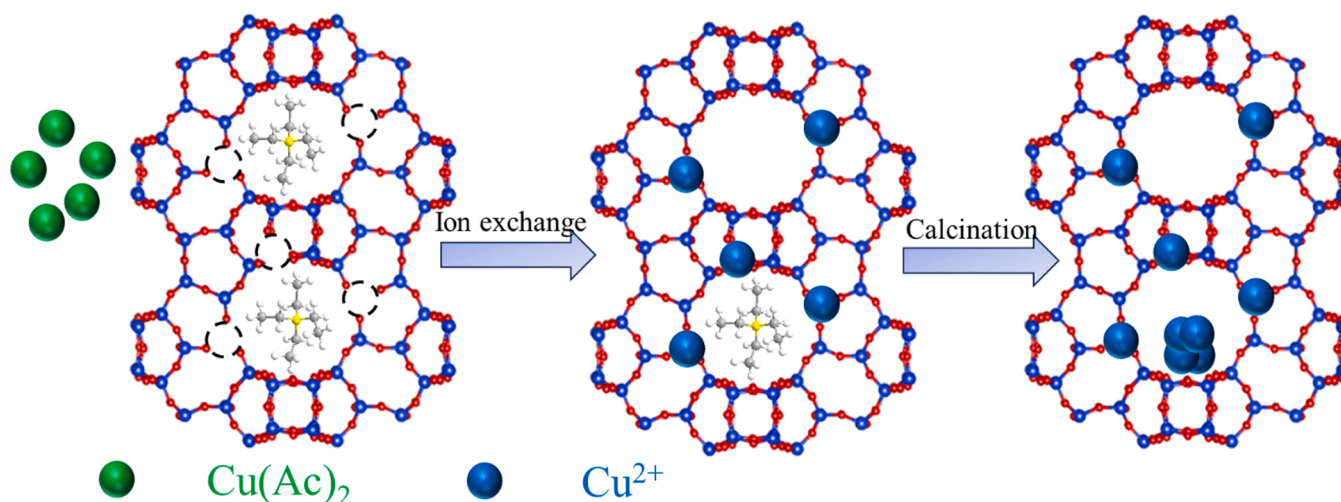
The PXRD patterns are collected to investigate the possible structural transformations in the ion-exchange process. the xCuSiBeta-IE samples were obtained through exchanging the Cu $^{2+}$ ions with SiBeta (the as-

synthesized *BEA-type pure-silica zeolite) directly (Scheme 1). As shown in Fig. 1a, the xCuSiBeta-IE displays a characteristic *BEA topology, suggesting that the Cu $^{2+}$ ions exchange process did not destroy the zeolite structures. Additionally, no distinct diffraction peaks attributable to copper species are evident in the 4.0/6.0/9.0CuSiBeta-IE samples across the range of copper loadings, indicating the high dispersion of copper species. After the calcination, there are still no obvious diffraction peaks of the copper species, which indicate their high distributions resulting from the stabilization by silicious zeolite matrix at elevated temperature (Fig. 2a). The N $_2$ physical adsorption results show that there is no discernible alteration in either surface area or micropore volume when compared to the calcined SiBeta sample, further corroborating the high dispersion of copper species within the pristine zeolite matrix (Fig. S2 and Table 1).

The Fourier transform infrared spectroscopy is also employed to probe the evolution of the silanol through the direct Cu $^{2+}$ ions exchange with the as-synthesized SiBeta. As shown in Fig. 1b, for the as-synthesized SiBeta, there is a distinct band appeared at 966 cm $^{-1}$ ascribed to silanol nests [37–39]. After exchange with the Cu $^{2+}$ ions, the intensity of band at 966 cm $^{-1}$ declines, which indicates the capture of the copper by the silanol nests. This observation is corroborated by ^{29}Si MAS NMR spectroscopy. As shown in Fig. 1c, for SiBeta, there are two principal signals with the chemical shift at -112.5 ppm and -102.5 ppm, which can be assigned to the Si(4Si) species and Si(3Si) species, respectively. After the ion-exchange with Cu(Ac) $_2$ solution, the chemical shifts of Si(4Si) species and Si(3Si) species slightly shift to -113.2 ppm and -102.6 ppm. Notably, there is a significant reduction in the intensities of the Si(3Si) species, which provides evidence that Cu $^{2+}$ ions have been effectively captured by the silanol nests within the zeolite matrix.

The chemical environment of Cu species in the 4.0/6.0/9.0CuSiBeta is probed by UV-vis spectroscopy (Fig. 2b). The energy associated with the oxygen-to-metal charge transfer can be utilized to assess the coordination of copper species within the zeolite matrix, which is contingent upon the number of surrounding oxygen atoms. For 4.0/6.0/9.0CuSiBeta, an absorption band appeared at 253 nm, which can be ascribed to the charge transfer between O $^{2-}$ and isolated mononuclear Cu $^{2+}$ species and oxidized copper clusters [30,40]. Moreover, there is no band in the range of 300 - 600 nm, indicating the absence of the bulk copper oxide. This finding aligns with the PXRD results and reveals the high dispersion of copper species throughout the zeolite matrix.

The reducibility of 4.0/6.0/9.0CuSiBeta samples is evaluated using H $_2$ -TPR experiments. The maximum reduction temperature is related to the interaction between Cu species and pure-silica matrix, as well as Cu contents. As shown in Fig. 2c, the reduction temperature of 4.0/6.0/



Scheme 1. Schematic illustration of the direct ion-exchange approach to prepare CuSiBeta samples.

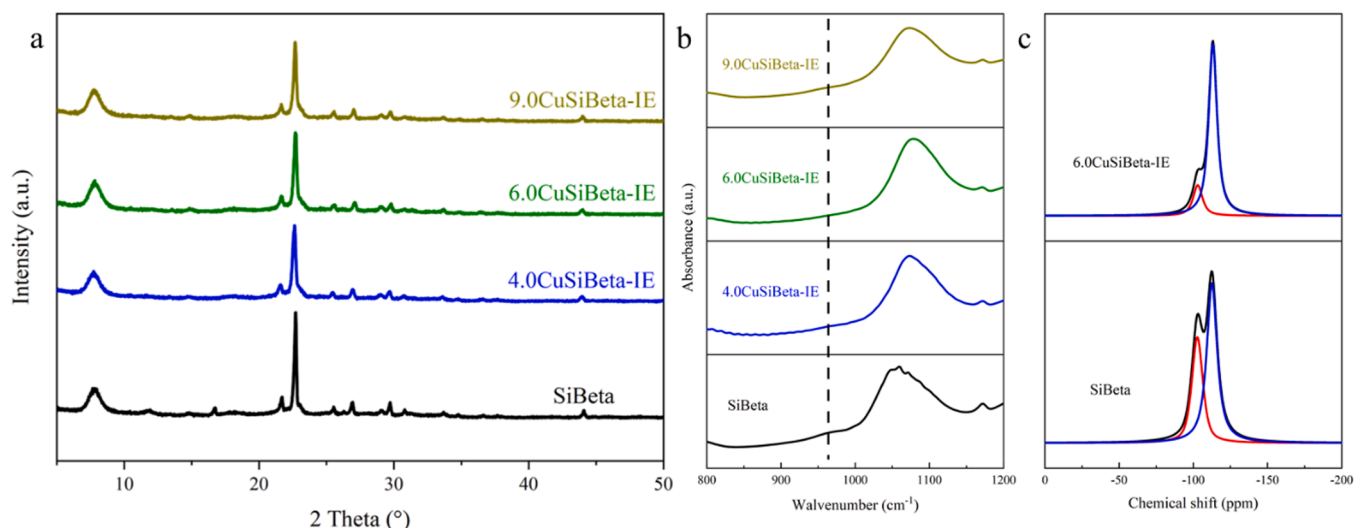


Fig. 1. (a) PXRD patterns of SiBeta and 4.0/6.0/9.0CuSiBeta-IE, (b) FTIR spectra of the SiBeta and 4.0/6.0/9.0CuSiBeta-IE, and (c) ²⁹Si MAS NMR spectra of the SiBeta and 6.0CuSiBeta-IE.

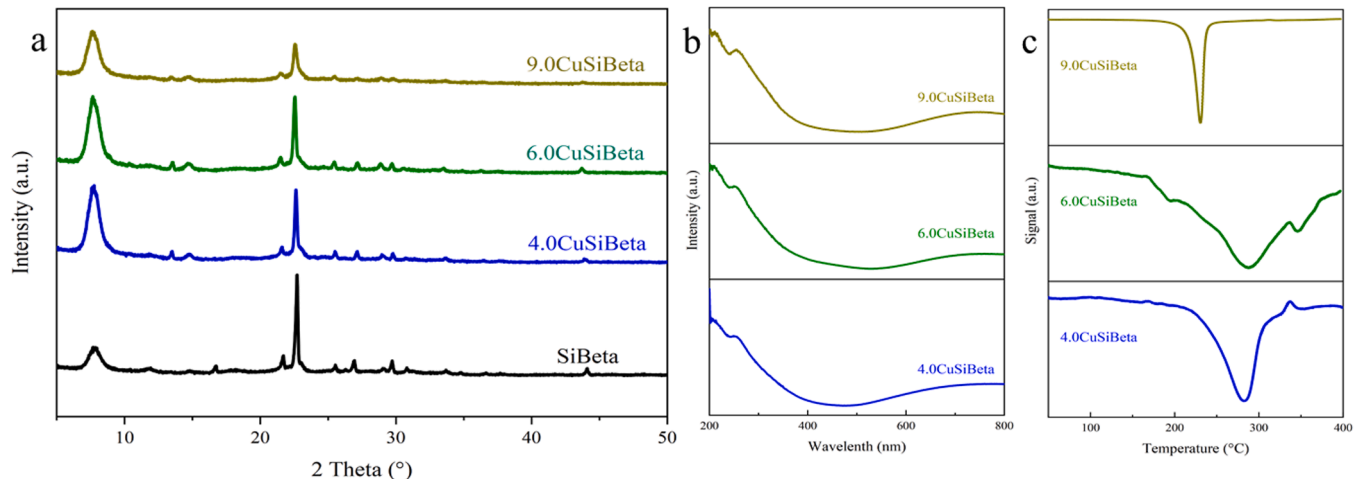


Fig. 2. (a) PXRD patterns of SiBeta and xCuSiBeta, (b) UV-vis spectra of xCuSiBeta and (c) H₂-TPR profiles of 4.0/6.0/9.0CuSiBeta.

Table 1

Cu loading and surface area of xCuSiBeta samples.

Samples	Cu loading (wt%) ^a	S _{BET} (m ² /g) ^c	V _{micro} (cm ³ /g) ^c	D _{Cu}
SiBeta-cal	—	480	0.194	
4.0CuSiBeta	4.0	527	0.218	0.64
6.0CuSiBeta	6.0	503	0.205	0.58
9.0CuSiBeta	9.0	462	0.199	0.25
6.0Cu/SiBeta-F	6.4 ^b	320	0.159	

^a Determined by XRF.

^b Determined by ICP-OES.

^c Determined by N₂-absorption.

9.0CuSiBeta samples prepared with the direct ion-exchange process decreases with increasing copper contents. The reduction peak of the 4.0CuSiBeta is observed at 283 °C, corresponding to the reduction of the copper oxide clusters [41,42]. When the copper loading is increased to 9.0 wt%, the reduction temperature drops to 230 °C, which may be because of the weaker interaction between copper species and zeolite matrix.

3.2. MSR catalytic performance of xCuSiBeta catalysts

Based on the preliminary characterization results, this series of 4.0/6.0/9.0CuSiBeta catalysts are utilized to test their MSR catalytic performance. The evaluations are conducted at 300 °C with a weight hour space velocity (WHSV) of 8.0 mL/g/h in N₂ atmosphere (34 mL/min). As shown in Fig. 3a, the conversion of methanol for 4.0CuSiBeta is 59% and the selectivity of H₂ and CO₂ are 75.2% and 24.8%, respectively. Increasing the Cu loading to 6 wt%, the methanol conversion raises up to 98%, meanwhile the selectivity of H₂ and CO₂ are 75.0% and 25.0%. There is no CO detected for the 4.0CuSiBeta and 6.0CuSiBeta at 300 °C. However, further increase the Cu loading to 9.0 wt%, the methanol conversion decline to 75% and the selectivity of H₂, CO₂, and CO are 74.6%, 24.6%, and 0.8%, respectively. The methanol conversion initially rises with the copper loading, but then decreases with the further increases in copper loading. The decline of methanol conversion and the increase of CO selectivity for 9.0CuSiBeta may be caused by the dispersion decrease of the copper species.

The durability of the 4.0/6.0/9.0CuSiBeta catalysts is investigated at 300 °C. For the 4.0CuSiBeta catalyst, the methanol conversion increases from 50% to 60% over the first 9 h and then stabilizes at 62%. Even after a TOS of 100 h, the methanol conversion remains at 60%. As shown in

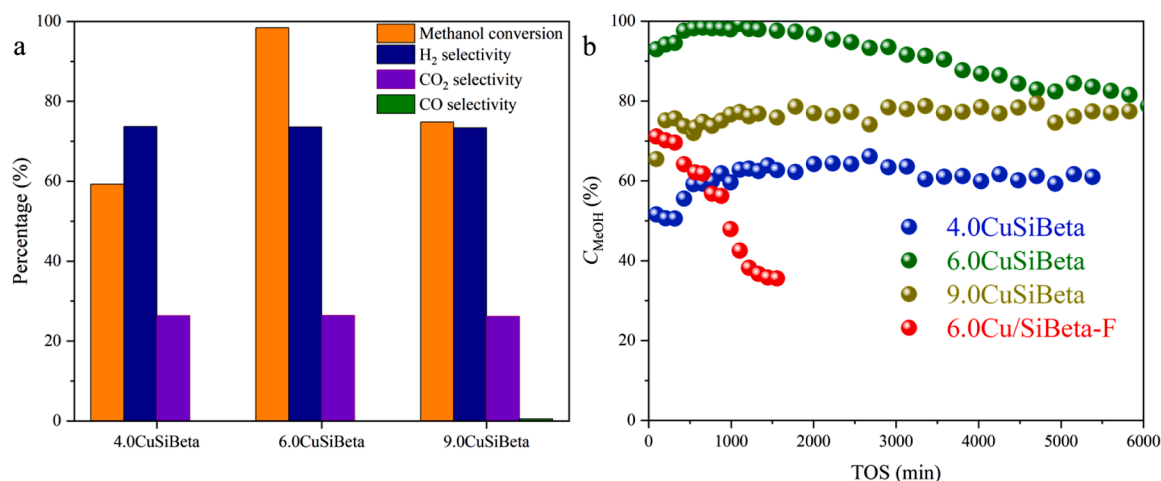


Fig. 3. (a) The effect of copper loading after a TOS of 11 h and (b) the durability of 4.0/6.0/9.0CuSiBeta and 6.0Cu/SiBeta-F samples at 300 °C in the MSR reaction. Reaction condition: WHSV= 8.0 mL/g/h, S/C= 2.26, N₂ flow rate: 34 mL/min, atmosphere.

Fig. 3b, the 6.0CuSiBeta exhibits better activity and stability with the methanol conversion rising from 93% to 98% over the initial 7 h and maintaining stability at 98% for 13 h. Subsequently, the methanol conversion slowly decreases, but it is still about 80% after a TOS of 100 h. Further increasing the copper loading to 9.0 wt% leads to a decline in the methanol conversion. Initially, the 9.0CuSiBeta catalyst displays a 73% methanol conversion, which then gradually increases to 77% over the following 20 h. After a TOS of 100 h, the methanol conversion was maintained at 76%. For comparison, another catalyst was prepared by the conventional impregnated methods and is denoted as 6.0Cu/SiBeta-F (detailed in the experimental section). Its initial methanol conversion is approximately 71%, which then decreases to 38% over the 20 h. The results indicate the 6.0CuSiBeta prepared by direct ion-exchange

exhibits superior methanol conversion and stability compared to 6.0Cu/SiBeta-F. The systematic investigations regarding 6.0Cu/SiBeta-F by PXRD, UV-vis spectrum, and H₂-TPR are also conducted, and it turns out that large copper oxide particles are the main copper species (details in Figs. S5, S7, and S8). The presence of the silanol nests in the SiBeta can enhance the dispersion of the copper species, inhibit their sintering, and further improve the methanol conversion and durability.

3.3. Evolution of copper species

We also characterize the spent 6.0CuSiBeta and 6.0Cu/SiBeta-F catalysts to understand the transformation of the catalysts before and after the reaction. PXRD patterns of both spent catalysts show that the

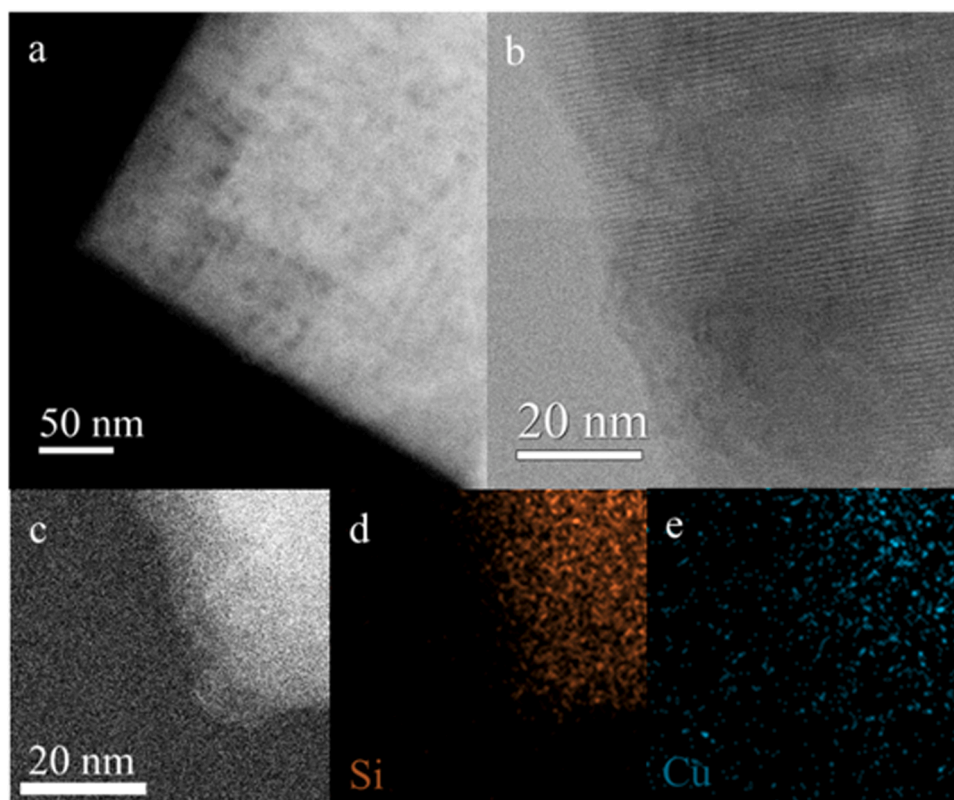


Fig. 4. (a) The STEM image, (b) TEM image, and (c–e) corresponding EDS mapping Si and Cu of 6.0CuSiBeta.

*BEA topology is preserved after the MSR reaction. It is of significance to point out that the spent 6.0CuSiBeta exhibited no diffraction peaks for copper or copper oxide, while spent 6.0Cu/SiBeta-F displays increased diffraction peak intensity at 43° due to reduced metallic copper with larger copper particles formed post-reaction. STEM and EDS mapping further confirm the higher dispersion and stability of copper species in the fresh 6.0CuSiBeta compared to 6.0Cu/SiBeta-F. As shown in Fig. 4, for the fresh 6.0CuSiBeta, there are no apparent copper oxide particles even clusters observed with clear lattice fringes of pure-silica zeolite, indicating the high dispersion of the copper species. For comparison, the STEM images of 6.0Cu/SiBeta-F reveal that there are obvious copper oxide particles on the surface of the fresh 6.0Cu/SiBeta-F, with particles of approximately 30 nm in size (Fig. S11). After the MSR reaction, the size of copper species increases to 5–10 nm after a TOS of 200 h for the spent 6.0CuSiBeta catalyst and the EDS mapping images show that there are still dispersed copper species existed (Fig. 5). However, for the 6.0Cu/SiBeta-F catalyst, the subsize copper species sinter severely with the size increase to 10–50 nm (Fig. S12). Therefore, direct ion-exchange method leads to highly dispersed copper species within the zeolite matrix, enhancing durability during the reaction.

XPS and the CO-FTIR spectroscopy were employed to investigate the existing states of the copper species in these catalysts. Before the MSR reaction, there are two main peaks around 936.3 eV and 956.1 eV in the fresh catalysts which can be assigned to Cu $2p_{3/2}$ and Cu $2p_{1/2}$, respectively. Additionally, an obvious satellite peak appeared at 944.3 eV is observed, indicating the presence of Cu $^{2+}$ in the 4.0/6.0/9.0CuSiBeta (Fig. 6a). The Cu $2p_{3/2}$ around 936.3 eV can be deconvoluted into separated peaks at 933.4 eV and 936.3 eV, which can be ascribed to copper oxide cluster and dispersed Cu $^{2+}$, respectively [43–45]. The binding energies at 935.67 eV and 956.30 eV in the Cu/SiBeta-F catalyst are associated with Cu $^{2+}$ species (Fig. 6a). Combined with the PXRD result, it indicates that the bulk copper oxide species have emerged in this catalyst. The existing states of the copper species in the 6.0CuSiBeta were further investigated using FTIR spectra

with the CO as probe molecule as shown in Fig. S13. Two bands appeared at 2133 and 2121 cm^{-1} , which can be ascribed to the adsorption of the CO to Cu $^+$ [21,26,46]. These results reveal that the interaction between the copper species and the zeolite matrix may lead to the formation of Cu $^+$.

As demonstrated in Fig. 6b, upon examination of the spent 4.0/6.0/9.0CuSiBeta catalysts, a shift is observed in the binding energy of the Cu $2p_{3/2}$ and Cu $2p_{1/2}$ to 933.0 eV and 953.0 eV, respectively. Concurrently, there is a significant reduction in the intensity of the associated satellite peaks, suggesting the formation of Cu 0 and/or Cu $^+$ species after the MSR reaction. The Cu $2p_{3/2}$ at 933.0 eV can be deconvoluted into two distinct peaks at 933.0 eV and 936.5 eV, which can be assigned to Cu $^+$ and/or Cu 0 as well as dispersed Cu $^{2+}$ [21,27,43,47]. For the spent xCuSiBeta samples, the presence of Cu $^+$ and/or Cu 0 indicates the nanosized copper oxide clusters in the zeolite matrix was reduced during the reaction, facilitated by the generation of H $_2$ in the MSR process. Meanwhile, the peak at 936.5 eV can be ascribed to the dispersed Cu $^{2+}$ for the spent 4.0/6.0/9.0CuSiBeta. However, for the spent 6.0Cu/SiBeta-F, the binding energy of Cu $2p_{3/2}$ varies to 932.7 eV, without a notable Cu $^{2+}$ satellite accompanied, indicating most of the copper oxides were reduced to Cu 0 and/or Cu $^+$. The PXRD pattern of the spent 6.0Cu/SiBeta-F shows that Cu 0 nanoparticles can be identified as shown in Fig. S9. Analysis of the Cu LMM AES spectra as presented in Fig. S14 reveals that the proportion of Cu $^+$ in the spent 4.0/6.0/9.0CuSiBeta samples diminish with an increase in copper content. The presence of Cu $^+$ in the spent 6.0CuSiBeta was also confirmed by CO-FTIR spectra, which revealed bands at 2132 and 2121 cm^{-1} corresponding to the adsorption of CO to Cu $^+$ sites (Fig. S15). Combining with the methanol conversion, the ratio of the (Cu 0 +Cu $^+$)/Cu $^{2+}$ (deduced from Fig. 6b) may determine the activity of the CuSiBeta catalysts. As (Cu 0 +Cu $^+$)/Cu $^{2+}$ increases, the conversion of methanol rises, and Cu $^+$ and Cu 0 work synergistically to enhance the MSR activity. Among the spent 4.0/6.0/9.0CuSiBeta catalysts, the 6.0CuSiBeta owns highest (Cu $^+$ +Cu 0)/Cu $^{2+}$ ratio, which leads to the highest methanol conversion

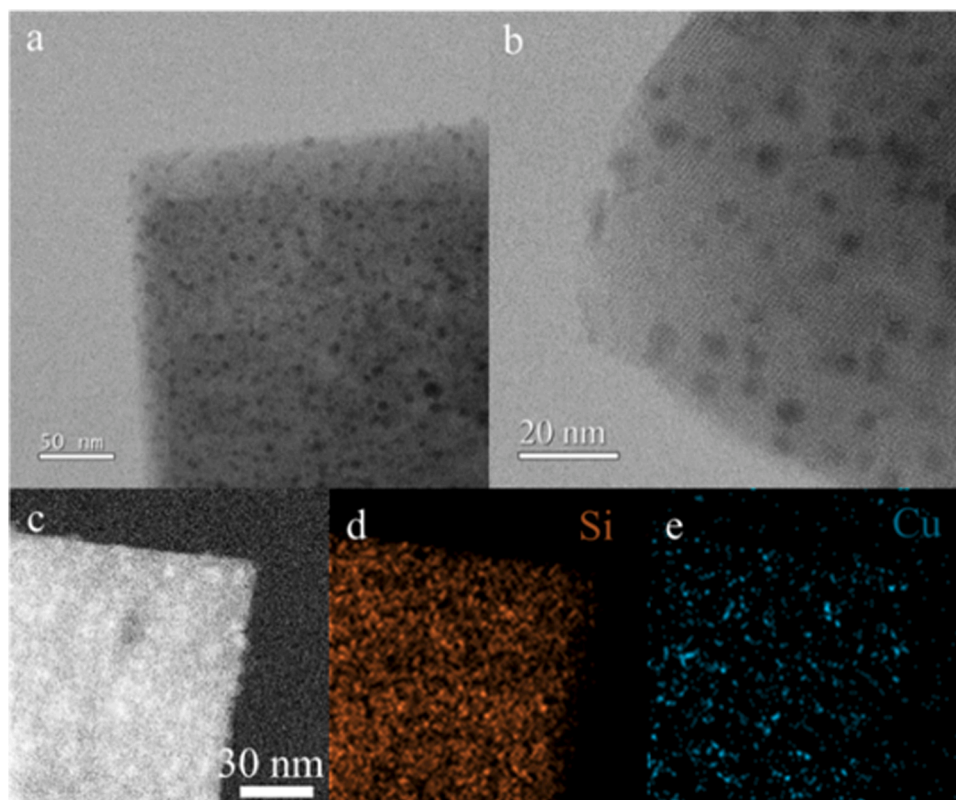


Fig. 5. (a, b) TEM images and (c–e) corresponding EDS mapping of Si and Cu of spent 6.0CuSiBeta.

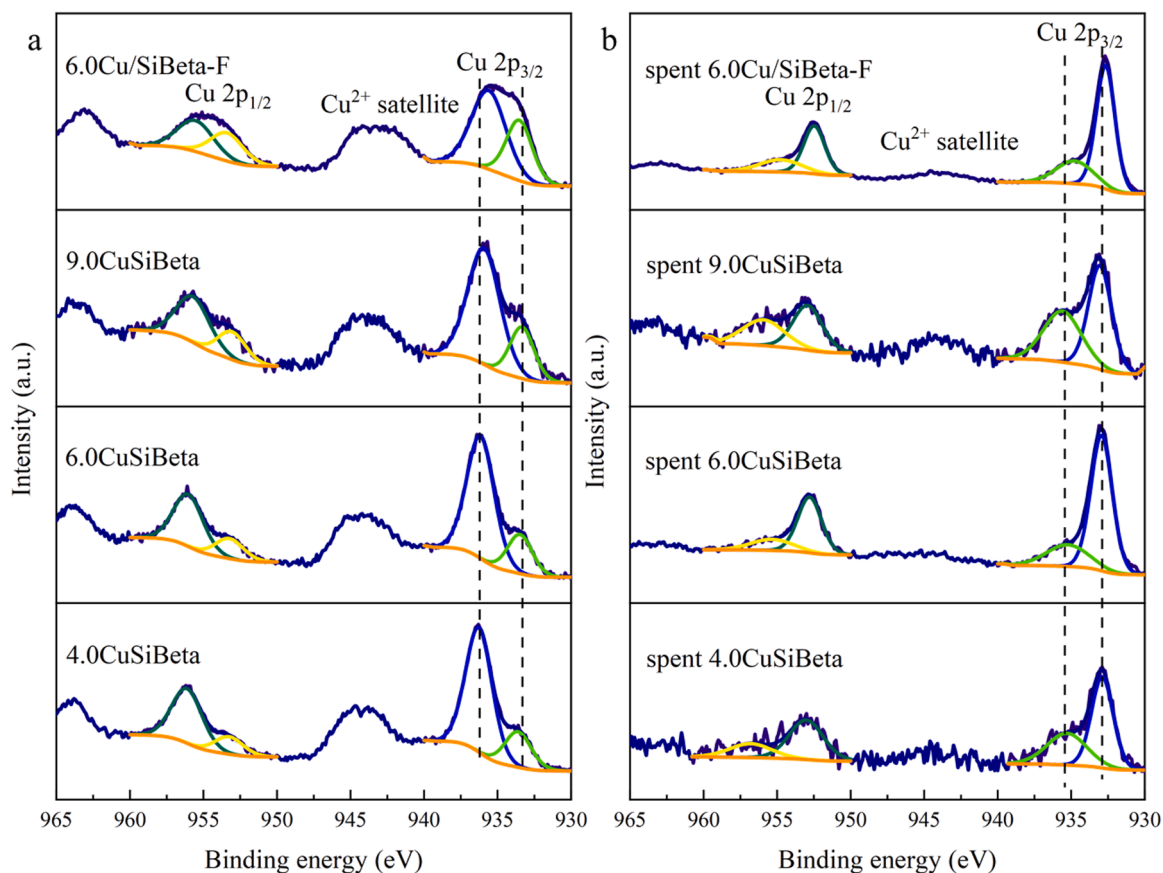


Fig. 6. (a) The Cu 2p XPS spectra of 4.0/6.0/9.0CuSiBeta and 6.0Cu/SiBeta-F samples and (b) Cu 2p XPS spectra of spent 4.0/6.0/9.0CuSiBeta and 6.0Cu/SiBeta-F.

in the TOS of 100 h. However, the ratio of $\text{Cu}^{2+}/(\text{Cu}^{+}+\text{Cu}^0)$ may impact the stability of the CuSiBeta catalysts; an increase ratio may improve the durability of the catalysts. The XPS and CO-FTIR analysis of the spent catalysts show that all the catalyst are reduced to Cu^0 and Cu^{+} , which work synergistically for the MSR reaction.

4. Conclusion

A series of xCuSiBeta MSR catalysts with high copper dispersion and high loading content have been successfully prepared by the direct ion-exchange method based on as-made *BEA-type pure-silica zeolite. Among these, the 6.0CuSiBeta catalyst maintains an 80% methanol conversion rate for a long lifetime of 100 h. The PXRD pattern, UV-vis spectra, and STEM images confirm the high dispersion of copper species within the 6.0CuSiBeta. This is primarily due to the silanol nests in the pure-silica zeolite matrix, which stabilize the copper species and enhance the catalyst's durability during the MSR reaction. Analysis of the spent catalysts using XPS and CO-FTIR spectra indicates that both Cu^0 and Cu^{+} species contribute synergistically to the MSR reaction.

CRediT authorship contribution statement

Yang Hong: Writing – original draft, Validation, Investigation, Formal analysis, Data curation. **Chao Ma:** Resources. **Nana Yan:** Writing – review & editing. **Peng Guo:** Writing – review & editing, Supervision, Resources, Project administration, Funding acquisition, Conceptualization. **Zhongmin Liu:** Supervision, Resources, Project administration, Funding acquisition.

Declaration of competing interest

The authors declare that they have no known competing financial

interests or personal relationships that could have appeared to influence the work reported in this paper.

Data availability

Data will be made available on request.

Acknowledgements

This work was supported by the National Natural Science Foundation of China (No. 22288101, 21972136, 21991090, 21991091, and 22102177).

Supplementary materials

Supplementary material associated with this article can be found, in the online version, at [doi:10.1016/j.mcat.2024.114436](https://doi.org/10.1016/j.mcat.2024.114436).

References

- [1] J.O. Abe, A.P.I. Popoola, E. Ajenifuja, et al., Hydrogen energy, economy and storage: review and recommendation, *Int. J. Hydrog. Energy* 44 (2019) 15072–15086, <https://doi.org/10.1016/j.ijhydene.2019.04.068>.
- [2] F. Dawood, M. Anda, G.M. Shafiqullah, Hydrogen production for energy: an overview, *Int. J. Hydrog. Energy* 45 (2020) 3847–3869, <https://doi.org/10.1016/j.ijhydene.2019.12.059>.
- [3] T. He, P. Pachfule, H. Wu, et al., Hydrogen carriers, *Nat. Rev. Mater.* 1 (2016) 16059, <https://doi.org/10.1038/natrevmats.2016.59>.
- [4] P.T. Aakko-Saksa, C. Cook, J. Kiviahho, et al., Liquid organic hydrogen carriers for transportation and storing of renewable energy—review and discussion, *J. Power Sources* 396 (2018) 803–823, <https://doi.org/10.1016/j.jpowsour.2018.04.011>.
- [5] S. Sá, H. Silva, L. Brandão, et al., Catalysts for methanol steam reforming—a review, *Appl. Catal. B* 99 (2010) 43–57, <https://doi.org/10.1016/j.apcatb.2010.06.015>.

- [6] S.T. Yong, C.W. Ooi, S.P. Chai, et al., Review of methanol reforming-Cu-based catalysts, surface reaction mechanisms, and reaction schemes, *Int. J. Hydrog. Energy* 38 (2013) 9541–9552, <https://doi.org/10.1016/j.ijhydene.2013.03.023>.
- [7] C.F. Shih, T. Zhang, J. Li, et al., Powering the future with liquid sunshine, *Joule* 2 (2018) 1925–1949, <https://doi.org/10.1016/j.joule.2018.08.016>.
- [8] L. Lin, W. Zhou, R. Gao, et al., Low-temperature hydrogen production from water and methanol using Pt/ α -MoC catalysts, *Nature* 544 (2017) 80–83, <https://doi.org/10.1038/nature21672>.
- [9] M. Nielsen, E. Alberico, W. Baumann, et al., Low-temperature aqueous-phase methanol dehydrogenation to iron catalyst and carbon dioxide, *Nature* 495 (2013) 85–89, <https://doi.org/10.1038/nature11891>.
- [10] L. Lin, Q. Yu, M. Peng, et al., Atomically dispersed Ni/ α -MoC catalyst for hydrogen production from methanol/water, *J. Am. Chem. Soc.* 143 (2021) 309–317, <https://doi.org/10.1021/jacs.0c10776>.
- [11] E.A. Bielinski, M. Förster, Y. Zhang, et al., Base-free methanol dehydrogenation using a pincer-supported iron compound and Lewis acid co-catalyst, *ACS Catal.* 5 (2015) 2404–2415, <https://doi.org/10.1021/acscatal.5b00137>.
- [12] E. Alberico, P. Sponholz, C. Cordes, et al., Selective hydrogen production from methanol with a defined iron pincer catalyst under mild conditions, *Angew. Chem. Int. Ed.* 52 (2013) 14162–14166, <https://doi.org/10.1002/anie.201307224>.
- [13] N. Köwitsch, L. Thoni, B. Klemmed, et al., Proving a paradigm in methanol steam reforming: catalytically highly selective In₂Pd₂/In₂O₃ interfaces, *ACS Catal.* 11 (2020) 304–312, <https://doi.org/10.1021/acscatal.0c04073>.
- [14] D. Li, Y. Li, X. Liu, et al., NiAl₂O₄ spinel supported Pt catalyst: high performance and origin in aqueous-phase reforming of methanol, *ACS Catal.* 9 (2019) 9671–9682, <https://doi.org/10.1021/acscatal.9b02243>.
- [15] H. Wang, Y. Hui, Y. Niu, et al., Construction of Pt^{δ+}-O(H)-Ti³⁺ species for efficient catalytic production of hydrogen, *ACS Catal.* 13 (2023) 10500–10510, <https://doi.org/10.1021/acscatal.3c02552>.
- [16] L. Liu, Y. Lin, Y. Hu, et al., ZnAl₂O₄ spinel-supported PdZn₀ catalyst with parts per million Pd for methanol steam reforming, *ACS Catal.* 12 (2022) 2714–2721, <https://doi.org/10.1021/acscatal.1c04922>.
- [17] C. Rameshan, W. Stadlmayr, S. Penner, et al., Hydrogen production by methanol steam reforming on copper boosted by zinc-assisted water activation, *Angew. Chem. Int. Ed.* 51 (2012) 3002–3006, <https://doi.org/10.1002/anie.201106591>.
- [18] F. Bossola, T. Roongcharoen, M. Coduri, et al., Discovering indium as hydrogen production booster for a Cu/SiO₂ catalyst in steam reforming of methanol, *Appl. Catal. B* 297 (2021) 120398, <https://doi.org/10.1016/j.apcatb.2021.120398>.
- [19] H. Li, H. Tian, S. Chen, et al., Sorption enhanced steam reforming of methanol for high-purity hydrogen production over Cu-MgO/Al₂O₃ bifunctional catalysts, *Appl. Catal. B* 276 (2020) 119052, <https://doi.org/10.1016/j.apcatb.2020.119052>.
- [20] Z. Shao, S. Zhang, X. Liu, et al., Maximizing the synergistic effect between Pt⁰ and Pt^{δ+} in a confined Pt-based catalyst for durable hydrogen production, *Appl. Catal. B* 316 (2022) 121669, <https://doi.org/10.1016/j.apcatb.2022.121669>.
- [21] Z. Cui, S. Song, H. Liu, et al., Synergistic effect of Cu⁺ single atoms and Cu nanoparticles supported on alumina boosting water-gas shift reaction, *Appl. Catal. B* 313 (2022) 121468, <https://doi.org/10.1016/j.apcatb.2022.121468>.
- [22] H. Yang, Y. Chen, X. Cui, et al., A highly stable copper-based catalyst for clarifying the catalytic roles of Cu⁰ and Cu⁺ species in methanol dehydrogenation, *Angew. Chem. Int. Ed.* 57 (2018) 1836–1840, <https://doi.org/10.1002/anie.201710605>.
- [23] T. Liu, C. Pei, T. Yang, et al., Promoted oxygen release from copper-ceria interfacial sites for selective hydrogen production, *Appl. Catal. B* 337 (2023) 123014, <https://doi.org/10.1016/j.apcatb.2023.123014>.
- [24] Y. Liu, H. Kang, X. Hou, et al., Sustained release catalysis: dynamic copper releasing from stoichiometric spinel CuAl₂O₄ during methanol steam reforming, *Appl. Catal. B* 323 (2023) 122043, <https://doi.org/10.1016/j.apcatb.2022.122043>.
- [25] P. Ribeirinha, C. Mateos-Pedrero, M. Boaventura, et al., CuO/ZnO/Ga₂O₃ catalyst for low temperature MSR reaction: synthesis, characterization and kinetic model, *Appl. Catal. B* 221 (2018) 371–379, <https://doi.org/10.1016/j.apcatb.2017.09.040>.
- [26] D. Li, F. Xu, X. Tang, et al., Induced activation of the commercial Cu/ZnO/Al₂O₃ catalyst for the steam reforming of methanol, *Nat. Catal.* 5 (2022) 99–108, <https://doi.org/10.1038/s41929-021-00729-4>.
- [27] F. Bossola, N. Scotti, F. Somodi, et al., Electron-poor copper nanoparticles over amorphous zirconia-silica as all-in-one catalytic sites for the methanol steam reforming, *Appl. Catal. B* 258 (2019) 118016, <https://doi.org/10.1016/j.apcatb.2019.118016>.
- [28] Y. Hong, Y. Zheng, N. Yan, et al., Cu nanoparticles confined in siliceous MFI zeolite for methanol steam reforming, *Catal. Sci. Technol.* 13 (2023) 6068–6074, <https://doi.org/10.1039/d3cy01165h>.
- [29] W. Dai, S. Zhang, Z. Yu, et al., Zeolite structural confinement effects enhance one-pot catalytic conversion of ethanol to butadiene, *ACS Catal.* 7 (2017) 3703–3706, <https://doi.org/10.1021/acscatal.7b00433>.
- [30] P.I. Kyriienko, O.V. Larina, S.O. Soloviev, et al., Ethanol conversion into 1,3-butadiene by the Lebedev method over MTaSiBEA zeolites (M = Ag, Cu, Zn), *ACS Sustain. Chem. Eng.* 5 (2017) 2075–2083, <https://doi.org/10.1021/acssuschemeng.6b01728>.
- [31] C. Chen, S. Zhang, Z. Wang, et al., Ultrasmall Co confined in the silanols of dealuminated beta zeolite: a highly active and selective catalyst for direct dehydrogenation of propane to propylene, *J. Catal.* 383 (2020) 77–87, <https://doi.org/10.1016/j.jcat.2019.12.037>.
- [32] D. Yu, W. Dai, G. Wu, et al., Stabilizing copper species using zeolite for ethanol catalytic dehydrogenation to acetaldehyde, *Chin. J. Catal.* 40 (2019) 1375–1384, [https://doi.org/10.1016/s1872-2067\(19\)63378-4](https://doi.org/10.1016/s1872-2067(19)63378-4).
- [33] T. Yan, W. Dai, G. Wu, et al., Mechanistic Insights into One-Step Catalytic Conversion of Ethanol to Butadiene over Bifunctional Zn–Y/Beta Zeolite, *ACS Catal.* 8 (2018) 2760–2773, <https://doi.org/10.1021/acscatal.8b00014>.
- [34] C. Ma, X. Liu, Y. Hong, et al., Fluoride- and seed-free synthesis of pure-silica zeolite adsorbent and matrix using OSDA-mismatch approach, *J. Am. Chem. Soc.* 145 (2023) 24191–24201, <https://doi.org/10.1021/jacs.3c08484>.
- [35] X. Zhao, L. Wang, P. Guo, et al., Synthesis of high-Si hierarchical beta zeolites without mesoporosity and their catalytic application in the methanol to propene reaction, *Catal. Sci. Technol.* 8 (2018) 2966–2974, <https://doi.org/10.1039/c8cy00631h>.
- [36] C.M.H.G.C. Chinchin, H.D. Vandervell, K.C. Waugh, The measurement of copper surface areas by reactive frontal chromatography, *J. Catal.* 103 (1987) 79–86, [https://doi.org/10.1016/0021-9517\(87\)90094-7](https://doi.org/10.1016/0021-9517(87)90094-7).
- [37] D. He, S. Wu, X. Cao, et al., Dynamic trap of Ni at elevated temperature for yielding high-efficiency methane dry reforming catalyst, *Appl. Catal. B* 346 (2024) 123728, <https://doi.org/10.1016/j.apcatb.2024.123728>.
- [38] T.D. Courtney, C.C. Chang, R.J. Gorte, et al., Effect of water treatment on Sn-BEA zeolite: origin of 960 cm⁻¹ FTIR peak, *Microporous Mesoporous Mater.* 210 (2015) 69–76, <https://doi.org/10.1016/j.micromeso.2015.02.012>.
- [39] L. Xie, Y. Chai, L. Sun, et al., Optimizing zeolite stabilized Pt-Zn catalysts for propane dehydrogenation, *J. Energy Chem.* 57 (2021) 92–98, <https://doi.org/10.1016/j.jechem.2020.08.058>.
- [40] P. Boroń, L. Chmielarz, S. Dzwigaj, Influence of Cu on the catalytic activity of FeBEA zeolites in SCR of NO with NH₃, *Appl. Catal. B* 168–169 (2015) 377–384, <https://doi.org/10.1016/j.apcatb.2014.12.052>.
- [41] L. Ding, T. Shi, J. Gu, et al., CO₂ hydrogenation to ethanol over Cu@Na-Beta, *Chem* 6 (2020) 2673–2689, <https://doi.org/10.1016/j.chempr.2020.07.001>.
- [42] Z.Q. Wang, Z.N. Xu, S.Y. Peng, et al., High-performance and long-lived Cu/SiO₂ nanocatalyst for CO₂ hydrogenation, *ACS Catal.* 5 (2015) 4255–4259, <https://doi.org/10.1021/acscatal.5b00682>.
- [43] J. Gong, H. Yue, Y. Zhao, et al., Synthesis of ethanol via syngas on Cu/SiO₂ catalysts with balanced Cu⁰-Cu⁺ sites, *J. Am. Chem. Soc.* 134 (2012) 13922–13925, <https://doi.org/10.1021/ja3034153>.
- [44] A. Rokicińska, P. Majerska, M. Drozdek, et al., Impact of Mn addition on catalytic performance of Cu/SiBEA materials in total oxidation of aromatic volatile organic compounds, *Appl. Surf. Sci.* 546 (2021) 149148, <https://doi.org/10.1016/j.apsusc.2021.149148>.
- [45] C. Zhou, H. Zhang, L. Yang, et al., Methane-selective oxidation to methanol and ammonia selective catalytic reduction of NO_x over monolithic Cu/SSZ-13 catalysts: are hydrothermal stability and active sites same? *Fuel* 309 (2022) 122178, <https://doi.org/10.1016/j.fuel.2021.122178>.
- [46] H. Meng, Y. Yang, T. Shen, et al., Designing Cu⁰-Cu⁺ dual sites for improved C–H bond fracture towards methanol steam reforming, *Nat. Commun.* 14 (2023) 7980, <https://doi.org/10.1038/s41467-023-43679-0>.
- [47] H. Zhang, H.R. Tan, S. Jaenicke, et al., Highly efficient and robust Cu catalyst for non-oxidative dehydrogenation of ethanol to acetaldehyde and hydrogen, *J. Catal.* 389 (2020) 19–28, <https://doi.org/10.1016/j.jcat.2020.05.018>.